



# A Size-Dependent Bonded-Particle Model for Transversely Isotropic Rock and its Application in Studying the Size Effect of Shale

Yun Zhao<sup>ID</sup> · Brijes Mishra<sup>ID</sup> · Qingwen Shi<sup>ID</sup> ·  
Gaobo Zhao<sup>ID</sup>

Received: 27 October 2021 / Accepted: 13 June 2022 / Published online: 5 July 2022  
© The Author(s), under exclusive licence to Springer Nature Switzerland AG 2022, corrected publication 2022

**Abstract** The bonded-particle model (BPM) method has been used to study the size effect and anisotropy of rock strength. This research proposes a new bonded-particle model which exhibits both size effect and anisotropy, for simulating transversely isotropic rocks. It assumes that transversely isotropic rocks consist of rock matrix, bedding planes, and randomly distributed cracks. Rock matrix is the base material which is isotropic and size independent, while bedding planes and cracks cause anisotropy and size effect respectively. The BPM of shale was developed in PFC2D. The BPM used bonded particles, smooth joints, and discrete fractures to model shale matrix, bedding planes, and cracks. The model introduced the three components and calibrated them progressively. At first, the matrix model was created, and its uniaxial compressive strength (UCS) was isotropic and size independent. Next, the bedding planes were introduced into the matrix model, and

the UCS became anisotropic. In the meantime, the cracks were introduced into the matrix model, and the UCS became size dependent. At last, the shale model was created by combining the shale matrix, bedding planes, and cracks. The UCS of shale model exhibited “U-shaped” curve and followed the decreasing asymptotic trend. The failure pattern of these models show that bedding planes cause anisotropy as they control the macroscopic failure, and the influence of bedding planes is pronounced irrespective of model size. Cracks cause size effect as they induce the localized failure, and the influence of cracks increases with the increase in model size. When the model size is small, anisotropy and size effect coexist. When the model size reaches a certain size, size effect disappears. The numerical result matches with the findings of published literature. The proposed model and its calibration procedure are applicable to other transversely isotropic rocks for analyzing the size effect and anisotropy.

Y. Zhao (✉) · B. Mishra · Q. Shi · G. Zhao  
Department of Mining Engineering, West Virginia  
University, 1374 Evansdale Drive, Morgantown,  
WV 26506, USA  
e-mail: yz0034@mix.wvu.edu

B. Mishra  
e-mail: brijes.mishra@mail.wvu.edu

Q. Shi  
e-mail: qs0003@mix.wvu.edu

G. Zhao  
e-mail: gz00001@mix.wvu.edu

**Keywords** Size effect · Transverse isotropic rock · Bonded-particle model · Uniaxial compressive strength

## 1 Introduction

Anisotropy and size effect significantly influence the strength properties of rock and rock mass. The anisotropy in rock causes the strength to vary with the

direction and the size effect influences the strength with the size of the test specimens. Both properties affect the estimation of rock mass strength from the result of standard-sized rock specimen. Shale is often considered as an anisotropic rock and is the immediate roof of the Appalachian underground coal mines. It is reported to have the highest rate of roof falls in the United States (Murphy 2016). The incorrect estimation of shale strength which often excludes anisotropy and size effect, has resulted in inadequate roof support design leading to roof fall problems (Arora and Mishra 2015; Bajpayee et al. 2014; Xue 2019).

Researchers have dealt with the anisotropy and size effect of rock strength since the early stage of rock mechanics. For some sedimentary and metamorphic rocks, the anisotropy is easily identified by visual inspection as they have bedding, foliation, or schistosity features, which are called the bedding planes. Specifically, shale is transversely isotropic with physical properties that are symmetric about the axis that is normal to the bedding planes. There are extensive experimental data that have reported strength anisotropy (Alliot and Boehler 1979; Attewell and Sandford 1974; Donath 1964; McLamore and Gray 1967; Niandou et al. 1997; Ramamurthy 1993). Duveau et al. (1998) summarized that the strength was maximum when the major stress was normal or parallel to bedding plane and the strength was minimum when the major stress and bedding planes was oriented between 30 and 60°. This strength variation with the orientation angle is referred as the “U-shaped” curve. To describe this “U-shaped” curve, numerous failure criteria have been proposed (Pei 2008). Among them, the single plane of weakness model is most extensively used (Jaeger 1960). Jaeger assumed that the bedding planes are weakness, and the rock failure occurs either along the bedding planes or inside the rock matrix. Unlike the anisotropy, the size effect of strength was noticed from the laboratory experimental result (Bieniawski 1968; Hoskins and Horino 1969; Mogi 1962; Pratt et al. 1972). Hoek and Brown (1980) statistically analyzed the published experimental data and concluded that the uniaxial compressive strength (UCS) decreased with increase in the specimen size, and the rate of decrease diminished above a certain size. To correlate this decreasing size effect, Hoek and Brown also proposed a power-law model (Hoek and Brown 1980), which was extensively used in rock engineering. Goodman (1989) explained the

size effect from the physical point of view. Goodman pointed out that the larger rock sample is more likely to contain flaws (cracks) in “critical locations”, thus it is more likely to fail under a certain stress state. Other than small-size rock, Kulatilake (2017) has conducted extensive research on anisotropic and size dependent strength of rock mass. He stated that the discontinuities in the rock mass makes the strength to be anisotropic and size dependent. He categorized the discontinuities into major and minor depending on the size. Major discontinuities (faults, bedding planes, and dikes) are considered as deterministically single features causing anisotropy. Minor discontinuities (fissures, fractures, and joints) are considered as randomly distributed features causing size effect. In summary, it is widely accepted that bedding planes causes the anisotropic strength and cracks cause the size dependent strength.

Shale, and other transversely isotropic rocks, contains bedding planes as the major discontinuities and cracks as the minor discontinuities. Therefore, these rocks should exhibit anisotropy and size effect at the same time. However, there are limited experimental data that have reported this combined anisotropy and size effect. Song et al. (2018) investigated the anisotropy and size effect on the UCS of coal. The UCS exhibits the “U-shaped” curve against the orientation angle for different-sized specimen. Though the decreasing size effect of UCS shows in all the orientation angles, the size effect is greatest when the orientation angle is 90° and is least when the orientation angle is 45°. Li et al. (2021) investigated the anisotropy and size effect on the triaxial compressive strength of slate. The triaxial compressive strength exhibits the “U-shaped” curve against the orientation and follow the decreasing size effect. The experimental study on the combined size effect and anisotropy is not available since tests need to be conducted on different-sized specimens at different orientations. The specimen preparation is time consuming, and the compression test is difficult to conduct for different-size specimens. Therefore, the investigation through laboratory experiment requires a large testing program which may not be economical.

The difficulties of the laboratory experiment are easily overcome using the numerical modeling technique. The challenge of numerical modeling is in creating a model that shows both the anisotropy and the size effect. For transversely isotropic rocks,

anisotropy and size effect are caused by bedding planes and cracks respectively. Then, the problem becomes how to introduce these discontinuities into numerical models. Kulatilake (2017) has performed pioneering research in using different numerical methods to generate the rock mass model with discontinuities. Kulatilake (1985) used the finite element method to generate the two-dimensional rock mass model that contains joints. This model successfully presents the anisotropy and size effect of rock mass. Kulatilake et al. (1992, 1993) used the distinct element method to create the two-dimensional and three-dimensional rock mass models with joints. They analyzed the influence of joint density, joint size, and joint orientation on the anisotropy and of size effect rock mass. They further developed the fracture tensor component to capture the influence of joint system and incorporated it into an incrementally linear elastic, orthotropic constitutive model. Kulatilake et al. (2001) used the bonded-particle model (BPM) to simulate the jointed rock blocks. They used spherical particles to model both intact rock and joints by assign different micro-mechanical properties. They also provided a realistic procedure for calibrating these properties based on the laboratory results. Compared with the finite element method and the distinct element method, the BPM method has the ability of simulating large displacement, large rotation, and progressive failure mechanism. In the past decades, the BPM method has been upgraded to model intact rock and discontinuities. As for intact rock, Potyondy (2012) proposed the flat-joint contact model for modeling the contact mechanism between bonded particles. This new contact model replicates many microstructural behaviors of intact rocks. As for minor discontinuities, Poulsen and Adhikary (2013) introduced cracks by randomly changing the contacts inside the BPM from bonded state to unbonded state. Their model successfully showed the size effect of UCS. They also found that the large sized model with high crack density had lower UCS. Zhang et al. (2011) modeled cracks as discrete fractures which were generated using the discrete fracture network (DFN) technique. The DFN technique stochastically generates discrete fractures based on their geometrical characteristics. The original contact that intersects with the discrete fractures were replaced with the smooth-joint contact model for simulating the mechanical behavior of cracks. Their model captured the size effect on UCS.

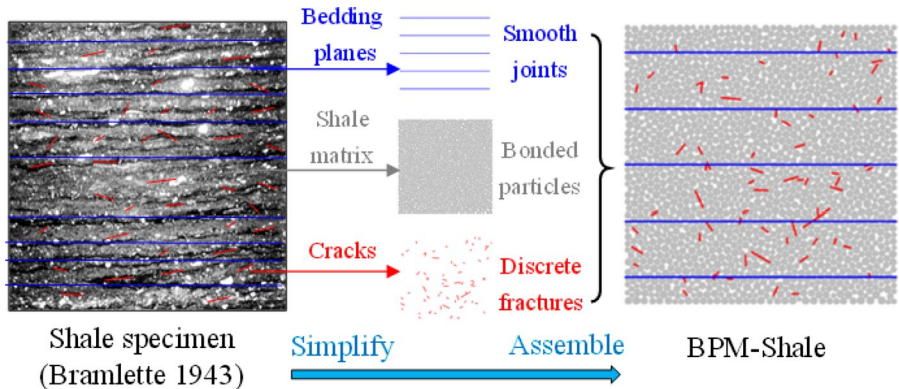
As for major discontinuities, Park and his colleagues (2015, 2018) used the smooth joint model to simulate the bedding planes in gneiss, shale, and schist. The numerical modeling result corresponded well with the anisotropic behavior of these rocks from laboratory observations. They also systematically verified the numerical modeling result with the analytical solutions. In summary, the BPM method and its embedded contact models have successfully been applied to model intact rock, minor discontinuities, and major discontinuities. However, there is limited research that has comprehensively investigated the anisotropy and size effect of rock strength.

The objective of this paper is to establish a new BPM for transversely isotropic rocks. This model should exhibit anisotropy and size effect. For this research, shale is selected for the rock type, and it is assumed that the anisotropy is caused by bedding planes and size effect is caused by randomly distributed cracks. The BPM of shale comprises three components: (1) shale matrix modeled by bonded particles, (2) bedding planes modeled by smooth joints, and (3) cracks modeled by discrete fractures. This study calibrated these three components in a progressive way. By applying the developed model, this study investigated the size effect and anisotropy of shale, which was helpful in estimating its field-scale strength for the roof stability analysis.

## 2 Methodology

As shown in Fig. 1, the structure of shale is simplified, consisting of shale matrix, parallel bedding planes, and randomly distributed cracks. Shale matrix is the base material which is assumed to be isotropic and size independent, while bedding planes and cracks are viewed as the major and minor discontinuities that cause the anisotropy and the size effect respectively. In the framework of PFC2D, shale matrix, bedding planes, and cracks are modeled using the bonded particles, smooth joints, and discrete fractures respectively. The assembly of bonded particles, smooth joints, and discrete fractures forms the BPM of shale (BPM-Shale).

**Fig. 1** The structure of shale and the BPM modeling technique



## 2.1 Calibration Procedure

It is impossible to generate the BPM-Shale directly by calibrating the microparameters of the bonded particles, smooth joints, and discrete fractures at the same time. Therefore, this study calibrated the three components in a progressive way:

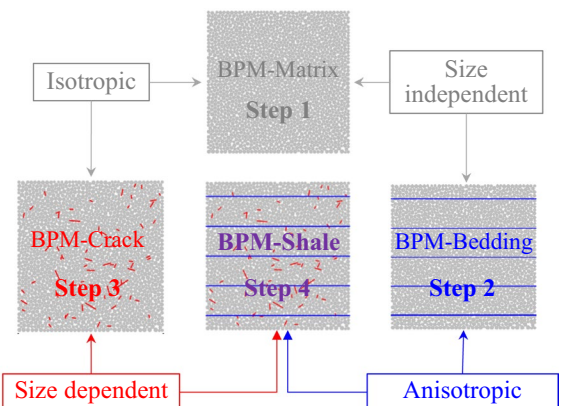
- (1) Step 1 generates the BPM of shale matrix (BPM-Matrix) and calibrates it so that the mechanical properties of the BPM-Matrix match those of shale matrix.
- (2) Step 2 creates the BPM of shale matrix with bedding planes (BPM-Bedding) by inserting smooth joints into the BPM-Matrix. It then calibrates the microparameters of smooth joints so that the BPM-Bedding shows the anisotropic mechanical behavior.
- (3) Step 3 creates the BPM of shale matrix with cracks (BPM-Crack) by inserting the discrete fractures into the BPM-Matrix. It then calibrates the microparameters of the discrete fractures so that the BPM-Crack presents the decreasing size effect of UCS.
- (4) Step 4 creates the BPM of shale (BPM-Shale) by adding the smooth joints and the discrete fractures into the BPM-Matrix. The BPM-Shale is used to study its anisotropy and size effect.

Fig. 2 shows the development procedure and the relationships between the BPM-Matrix, BPM-Bedding, BPM-Crack, and BPM-Shale. Without loss of generality, this study calibrated the anisotropic behavior at the orientation  $\beta$  of  $0^\circ$ ,  $45^\circ$ , and  $90^\circ$ , and it calibrated the size effect at the size  $D$  of 25, 50, 75,

100, 125, 150, and 200 mm. Fig. 3 shows the model generation schedule of BPM-Matrix, BPM-Bedding, BPM-Crack, and BPM-Shale.

## 2.2 Mechanical Properties of BPM Models

This study calibrated the microparameters of bonded particles, smooth joints, and discrete fractures based on the mechanical properties of BPM-Matrix, BPM-Bedding, and BPM-Crack, respectively. The BPM-Matrix is the intact part of shale, which has the highest deformation modulus and strength. The deformation modulus and strength of BPM-Bedding are anisotropic due to the smooth joints. The BPM-Crack shows the decreasing size effect of UCS due to the discrete fractures. It is difficult to derive the mechanical properties of the BPM models based on the experiment result of shale. Instead, we set



**Fig. 2** Development procedure and the relationships between BPM-Matrix, BPM-Bedding, BPM-Crack, and BPM-Shale

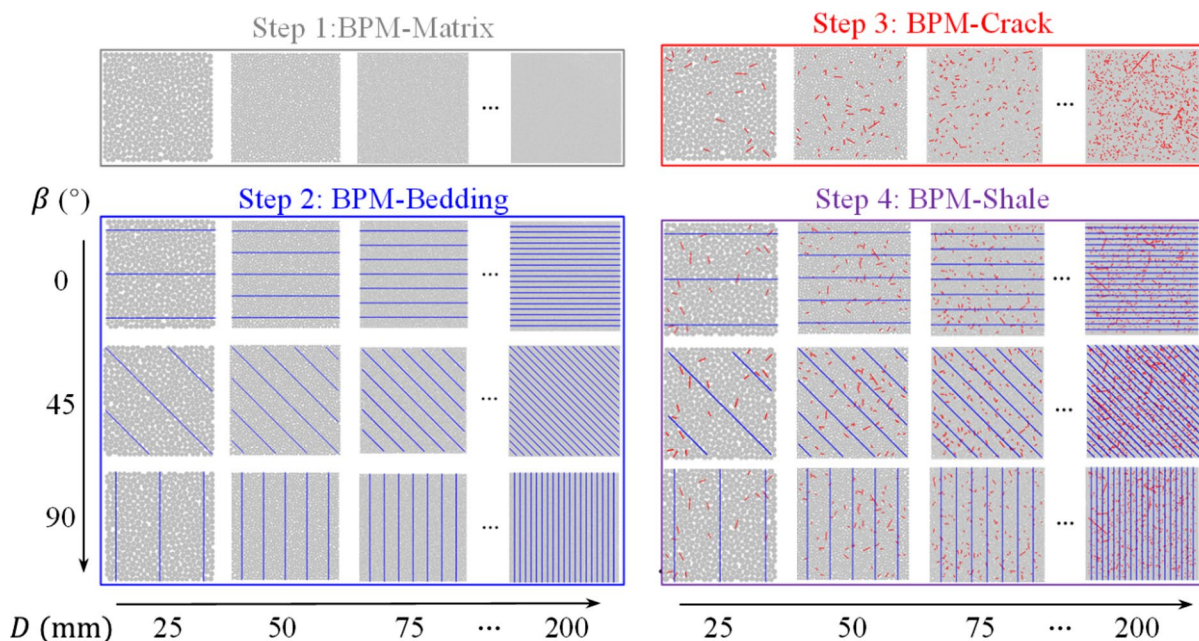


**Fig. 3** Schematic view of the model generation schedule

**Table 1** Mechanical properties of BPM-Matrix and BPM-Beddings

Specimen type	E (GPa)	UCS (MPa)	DTS (MPa)
BPM-matrix	38.81	64.92	9.12
BPM-bedding ( $0^\circ$ )	16.53	61.82	2.73
BPM-bedding ( $45^\circ$ )	21.18	47.68	4.97
BPM-bedding ( $90^\circ$ )	36.96	57.39	8.69

appropriate mechanical properties for the BPM models. We assumed that through the calibration of the BPM models, the assembly of bonded particles, smooth joints, and discrete fractures (BPM-Shale) can closely represent shale specimens in the laboratory.

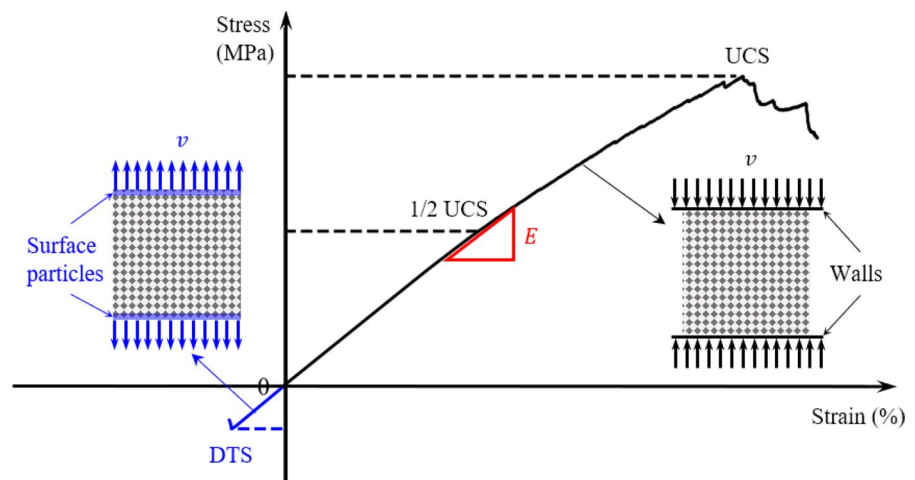
Table 1 lists the mechanical properties of BPM-Matrix and BPM-Bedding at the size of 50 mm. The Young's modulus and direct tensile strength (DTS) of BPM-Matrix was set 5% higher than that of the BPM-Bedding with the orientation of  $90^\circ$ , and the UCS of the BPM-Matrix was set 5% higher than the value of BPM-Bedding with the orientation of  $0^\circ$ . These properties selected here is just an example from (Jin et al. 2018). In fact, other set of properties can be used as long as they can reflects the anisotropy of rock. For

BPM-Crack, the UCS is lower than BPM-Matrix, and it should decrease with the increase of model size.

### 2.3 Calibration Setup

This study conducted the model calibration through the uniaxial compression test and the direct tension test. Fig. 4 shows the uniaxial compression and the direct tension test setup and a typical stress-strain curve. In the uniaxial compression test, a pair of frictionless grid walls is used as the loading platens. In the direct tension test, the top and bottom surface particles of the model are fixed to act as the loading platens. During the tests, the rate of loading is maintained at a level to ensure a quasi-static load on the model. The stress is measured as the wall force divided by the cross-sectional area of model, while the strain is measured as the change of distance between opposing walls (Potyondy 2019). The Young's modulus is calculated as the tangent modulus at the stress level that is 50% of the UCS. The model genesis and test procedure follow “Material-Modeling Support for PFC [fistPkg6.6]” (Potyondy 2019).

**Fig. 4** Typical stress–strain curves of the uniaxial compression test and direct tension test



### 3 Result

#### 3.1 BPM-Matrix

In the BPM-Matrix, this study selected the flat-joint model for simulating the contact mechanism between bonded particles. The flat-joint model has the advantage of matching the large UCS/DTS ratio and replicating many microstructural behaviors of rocks (Potyondy 2018). Table 2 shows the determined microparameters of BPM-Matrix. Fig. 7 shows the stress–strain curve of the calibrated BPM-Matrix. The Young's modulus, UCS, and DTS are 38.79 GPa, 64.89 MPa, and 8.99 MPa respectively. The mechanical properties of BPM-Matrix agree well with those in Table 1.

To check the size independence on its UCS, the BPM-Matrix was scaled to the sizes of 25, 75, 100, 125, 150, and 200 mm. It is important to note the randomness of generating particles. It causes the packing arrangement of particles varied with the change in the model size. To eliminate the influence of randomness, this study created 10 realizations for each model size by varying the random seed from 1 to 10, then used the average value of the 10 realizations for analyzing the size effect on the UCS. Thus, there were 7 differently sized models and their 10 realizations. Fig. 5 shows the uniaxial compression test results of the BPM-Matrix: (a) variation of UCS with model sizes, and (b) displacement magnitude of failed BPM-Matrix of 50, 100, and 150 mm at random seed 1. From Fig. 5(a), the dispersion of UCS exhibits no clear change with increasing model size.

**Table 2** Microparameters properties of the BPM-Matrix

Microparameter*	Value
<i>Common group</i>	
$\alpha, C_a, \rho_v [\text{kg/m}^3]$	0.7, 1, 2558
$S_g, T_{SD}, \{D_{\{l,u\}} [\text{mm}], \phi\}, D_{mult}$	0, 0, {1.0, 1.6, 1.0}, 1.0
<i>Packing group</i>	
$P_m [\text{MPa}], \varepsilon_p, \varepsilon_{lim}, n_{lim}$	$30, 1 \times 10^{-2}, 8 \times 10^{-3}, 2 \times 10^6$
$C_p, n_c$	1, 0.08
<i>Flat-jointed material group</i>	
$C_{MS}, g_i [\text{mm}], \phi_B, \phi_{G_i}, (g_o)_{\{m,sd\}}$ [mm], [ $N_r, N_g$ ]	False, 0.15, 1, 0, {0, 0}, 2 {0, 1}, 45, 3.6, 0.4
$\{C_\lambda, \lambda_v\}, E^* [\text{GPa}], \kappa^*, \mu$	{13.8, 0}, {37, 0}, 30
$(\sigma_c)_{\{m,sd\}} [\text{MPa}], (c)_{\{m,sd\}} [\text{MPa}],$ $\phi [\text{degrees}]$	
<i>Linear material group</i>	
$E_n^* [\text{GPa}], \kappa_n^*, \mu_n$	45, 3.6, 0.4

\* The Microparameters are defined in Potyondy (2019)

The average value of UCS is almost independent of model size, except for the small difference at 25 mm. Fig. 5(b) presents the displacement of particles in the grayscale image, where the darkness represents the displacement magnitude. The differences in darkness indicate the relative shear displacement along a plane, where the failure occurs. In general, the failure pattern is oblique shear, and it is independent of model size. Fig. 6 compares the failure mode for the 100 mm BPM-Matrix at random seed from 1 to 5. It shows that all the models present the oblique shear though the failure location varies. The similarity of failure mode at different random seed applies to other-size models, though only the 100 mm BPM-Matrix is

presented here as an example. In summary, the failure pattern of BPM-Matrix is oblique shear, it is independent of model size, and the influence of random seed is limited.

### 3.2 BPM-Bedding

This study modeled bedding planes using smooth joints, which were added by replacing the flat-joint model between particles with the smooth-joint contact model. The smooth-joint model has the advantage of overcoming the inherent roughness problems of particles (Itasca Consulting Group 2019).

Table 3 presents the determined microparameters of the smooth joints model. Fig. 7 compares the stress-strain curves of BPM-Bedding and BPM-Matrix. The Young's modulus, UCS, and DTS of BPM-Bedding at the orientation of 0° (BPM-Bedding-0) are 16.46 GPa, 61.47 MPa, and 2.78 MPa respectively. The Young's modulus, UCS, and DTS of BPM-Bedding-45 are 22.42 GPa, 47.90 MPa, and 4.59 MPa respectively. The Young's modulus, UCS, and DTS of BPM-Bedding-90 are 36.37 GPa, 54.20 MPa, and 8.71 MPa respectively. In general, the mechanical properties of BPM-Bedding match well with those in Table 1.

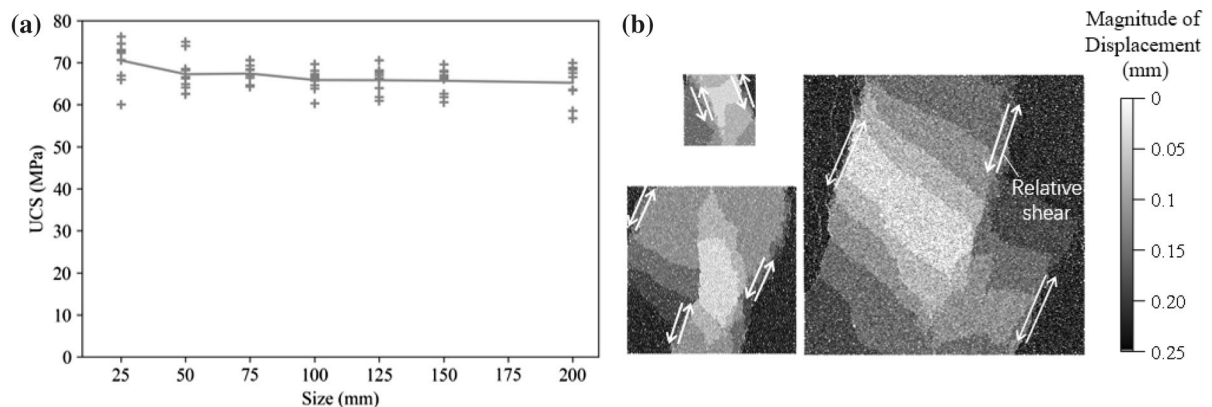


**Fig. 5** Uniaxial compression test results of the BPM-Matrix: **a** variation of UCS with different model sizes, **b** displacement magnitude of failed models of 50, 100, and 150 mm at random seed 1

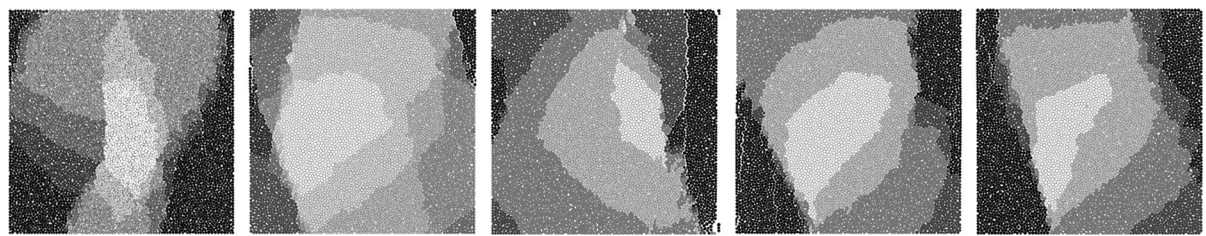


**Fig. 6** Failure mode comparison for the 100 mm BPM-Matrix at random seed from 1 to 5 (from left to right)

**Table 3** Microparameters of the smooth joint model

Normal stiffness (GPa/m)	Shear stiffness (GPa/m)	Friction coefficient	Friction angle (°)	Tensile strength (MPa)	Cohesion (MP)	Spacing (mm)
1750	1750	0.4	30	2.2	13.5	10

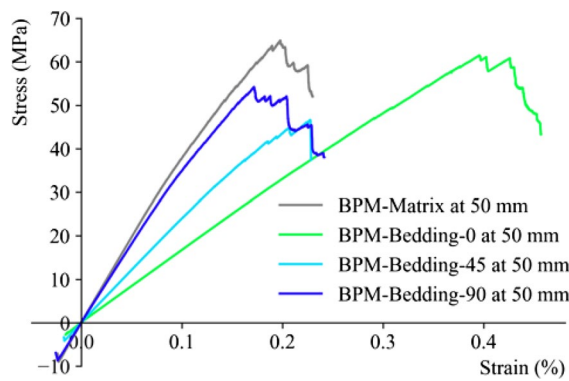


**Fig. 7** Stress–strain curves of calibrated BPM-Matrix and BPM-Bedding at the size of 50 mm

The BPM-Bedding models were scaled to the sizes of 25, 75, 100, 125, 150, and 200 mm to check the size independence. This study created 10 realizations for each model of the specific size and orientation. The average value of the 10 realizations was

used for analyzing the size effect on the UCS. Fig. 8 shows the uniaxial compression test results of the BPM-Bedding: (a) variation of UCS with model sizes and orientation, (b) displacement magnitude of failed BPM-Bedding-0 at random seed 1, (c) displacement magnitude of failed BPM-Bedding-45 at random seed 1, and (d) displacement magnitude of failed BPM-Bedding-90 at random seed 1. From Fig. 8(a), there was no observable change in the UCS dispersion with the increase in the model size at various orientations. As shown in Figs. 8(b)–(d), the displacement magnitude of the failed BPM-Bedding demonstrates that the failure pattern is dependent on the orientation of the bedding plane. When the orientation is  $0^\circ$ , the failure pattern of BPM-Bedding is similar to the BPM-Matrix. The results showed the oblique shear failure inside shale matrix and across the bedding planes. When the orientation is  $45^\circ$ , relative displacement occurs at the bedding planes, which indicates

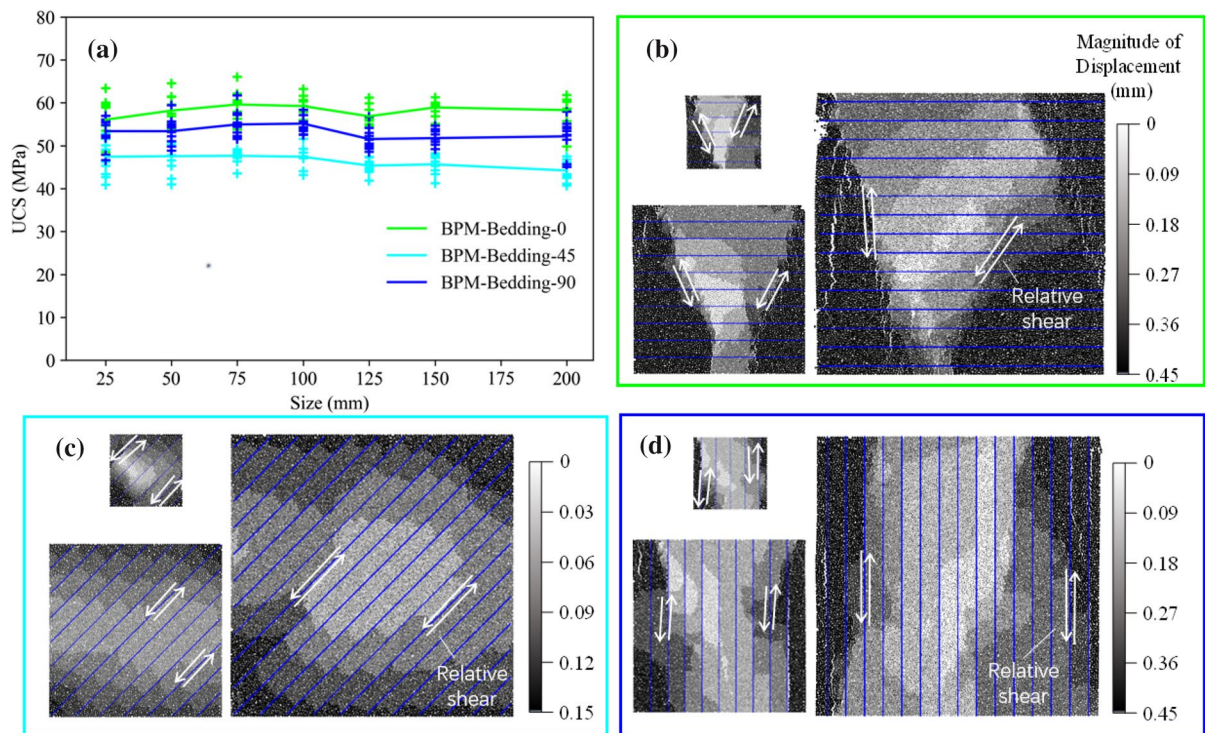


**Fig. 8** Uniaxial compression test results of the BPM-Bedding: **a** variation of UCS with different model sizes and orientations, **b** displacement magnitude of failed BPM-Bedding-0 at random

seed 1, **c** displacement magnitude of failed BPM-Bedding-45 at random seed 1, **d** displacement magnitude of failed BPM-Bedding-90 at random seed 1

the shear failure along bedding planes. When the orientation is 90°, the failure pattern is tensile splitting along bedding planes. Fig. 9 compares the failure mode for the 100 mm BPM-Bedding-0, BPM-Bedding-45, and BPM-Bedding-90 at random seed from 1 to 5. Regarding the change of random seed, the BPM-Bedding-0 shows the oblique shear failure inside shale matrix, the BPM-Bedding-45 shows the shear failure along bedding planes, and the BPM-Bedding-90 shows the tensile splitting along bedding planes. In summary, the failure pattern of BPM-Bedding is affected by the orientation and is independent of the model size. The influence of the random seed is limited.

### 3.3 BPM-Crack

This study modeled cracks using the discrete fractures, whose mechanical behavior is simulated as broken shale matrix. Thus, cracks inherited the same microparameters of shale matrix except that the tensile strength and cohesion were set as 0. The discrete fractures were generated using the DFN technique

based on the geometrical properties of cracks such as position, orientation, size, and density. Research has widely accepted that the position and orientation cracks are randomly distributed in rocks (Cundall et al. 2008; Poulsen and Adhikary 2013). The size and density of cracks are the factors causing the size effect, as a larger specimen is more likely to contain larger cracks; thus it is more likely to fail (Goodman 1989; Griffith 1924). Bonnet et al. (2001) summarized that the power law distribution provides a widely applicable characterization for the size and density of cracks. The relationship of crack density and size is  $n(l) = \alpha \times l^{-c}$ , where  $l$  is the crack size,  $n(l)$  is the number of cracks with the size in the range  $[l, l + dl]$ ,  $\alpha$  is the density constant, and  $c$  is the scaling exponent. The size distribution of cracks is between the lower bound  $l_{min}$  and upper bound  $l_{max}$ .

In this study, the value of  $l_{min}$  was set as the smallest size of particles, since the smallest crack exists at the boundary of the smallest particles. The value of  $l_{max}$  was changing with the model size, which indicates that the larger model is more likely to contain large cracks. The density constant  $\alpha$  and the scaling

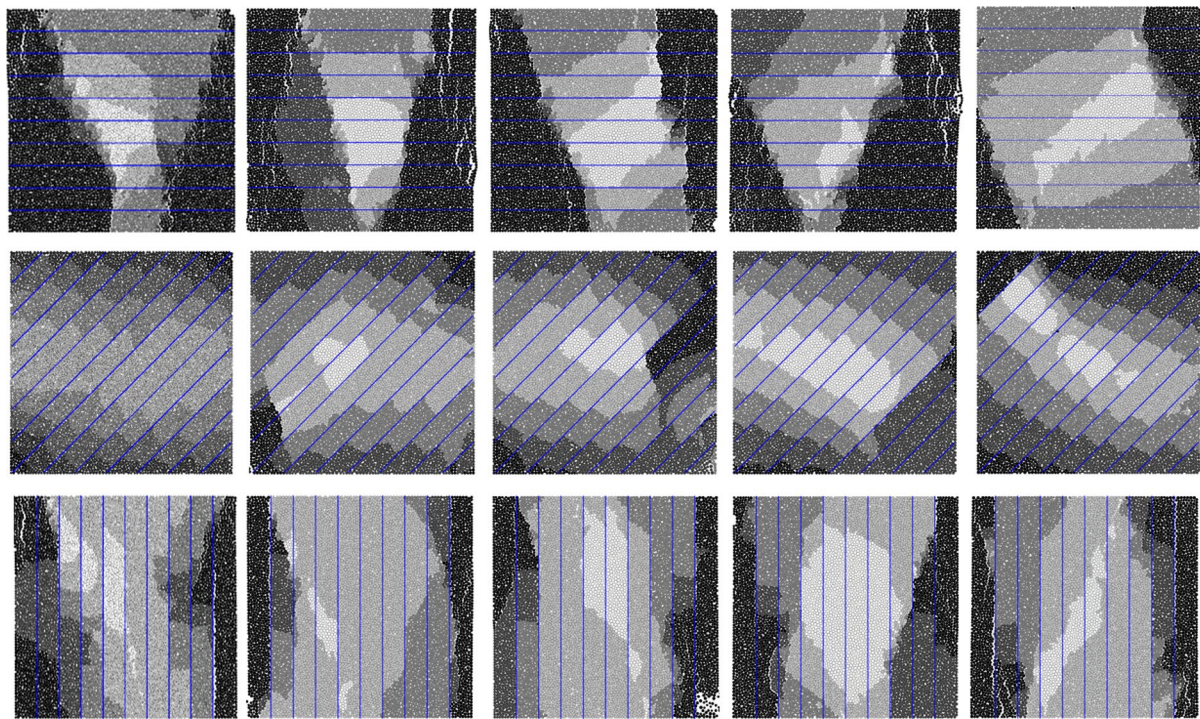


**Fig. 9** Failure mode comparison for the 100 mm BPM-Bedding-0, BPM-Bedding-45, and BPM-Bedding-90 at random seed from 1 to 5 (from left to right)

**Table 4** Parameters of the power-law distribution of crack size and density

Parameter	$\alpha$ (mm/mm <sup>2</sup> )	$c$	$l_{min}$ (mm)	$l_{max}$ (mm)
Value	5000	3	1	Model size

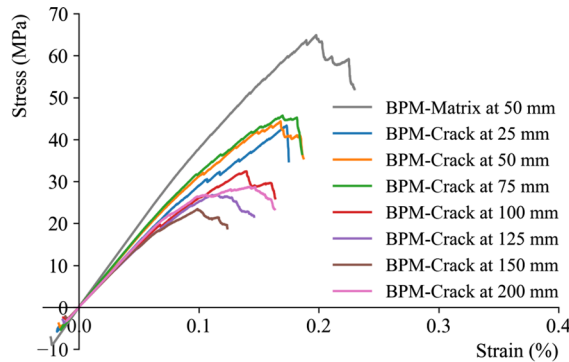


**Fig. 10** Stress–strain curves of calibrated BPM-Bedding at different sizes

exponent  $c$  were adjusted so that the BPM-Crack shows the decreasing size effect on UCS. Table 4 shows the determined parameters of the power-law distribution of crack size and density after calibration. Fig. 10 compares the calibration result of BPM-Crack at different sizes and adds the result of BPM-Matrix for the convenience of comparison. This figure shows that the introduction of cracks decreases the Young's modulus, UCS, and DTS. Furthermore, the value of Young's modulus, UCS, and DTS decreases as the

model size increases in the general case. The decreasing trend is not strictly applied in the cases of 25, 50, and 200 mm. The cause of this anomaly is the randomness of generating cracks. To avoid this anomaly, the average value of 10 realizations was used to study the size effect.

Fig. 11 shows the uniaxial compression test results of the BPM-Crack: (a) variation of UCS with model sizes, and (b) displacement magnitude of failed BPM-Crack of 50, 100, and 150 mm at random seed 1. From Fig. 11(a), the dispersion of the UCS of BPM-Crack is much more prominent than those of BPM-Matrix and BPM-Bedding. Unlike the constant dispersion in BPM-Matrix and BPM-Bedding, the dispersion in BPM-Crack decreases with the increase of model size. The change of random seed alters the configuration of cracks as shown in Fig. 12. When the model size is small and contains only a few cracks, the UCS varies considerably when the random seed changes. As the model size increases to contain more cracks, the model becomes more homogeneous regarding the configuration of cracks. Therefore, the UCS variability decreases as model size increases. More important, the result clearly shows the decreasing size effect on the UCS. The average value of UCS decreased from around 45 MPa to 30 MPa when the model size increased from 25 to 200 mm, and the decreasing rate of UCS diminished as model size increased. According to Fig. 11(b), the cracks affected the displacement magnitude of failed BPM-Crack. The relative shear displacement occurred around the crack and caused localized failure. Moreover, the localized

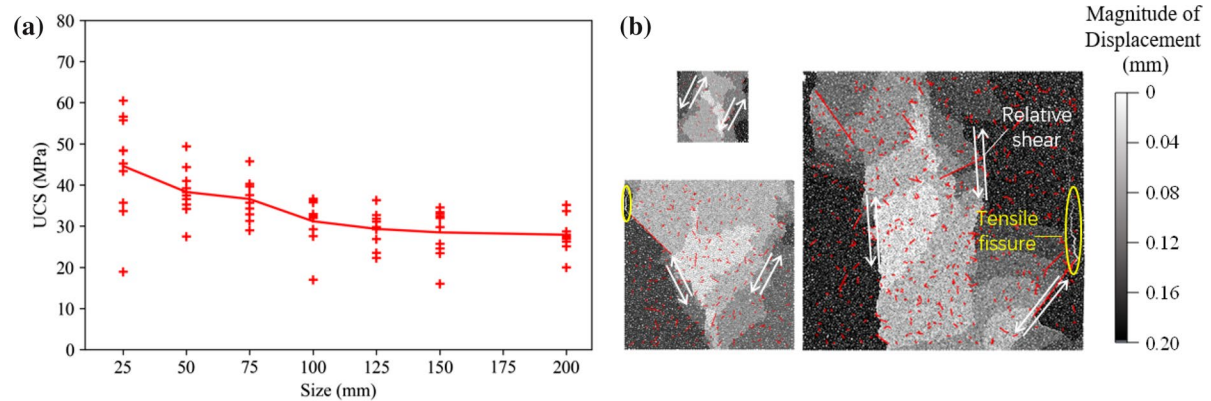


**Fig. 11** Uniaxial compression test results of the BPM-Crack: **a** variation of UCS with different model sizes, **b** displacement magnitude of failed models of 50, 100, and 150 mm at random seed 1

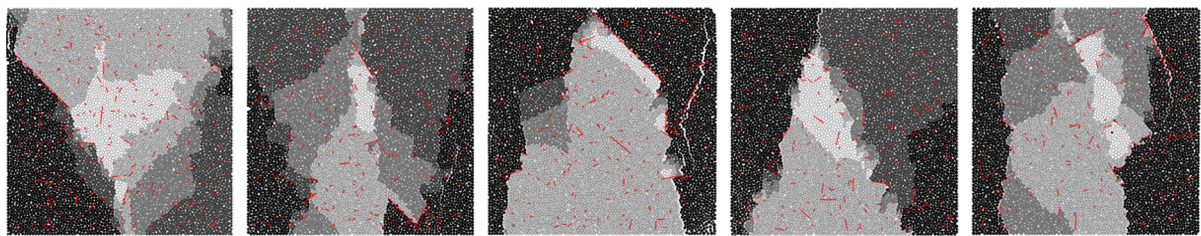


**Fig. 12** Failure mode comparision for the 100 mm BPM-Crack at random seed from 1 to 5 (from left to right)

failure initialized the tensile fissure. The localized failure and tensile fissure were close the largest crack, which demonstrates that larger cracks have higher influence. As larger model is more likely to contain larger cracks, it has lower UCS. But the crack length is restricted by the power law distribution as the crack number  $n(l)$  decreases very quick when the crack length  $l$  increases. When the model size increases to a certain size (125 mm here), the increase of large cracks becomes negligible and the decrease rate of UCS diminishes. It is important to note that all the models present the oblique shear regardless of the size, though the cracks can cause small tensile fissure. Fig. 12 compares the failure mode for the 100 mm BPM-Crack at random seed from 1 to 5. It shows that the change of random seed affects the crack configuration, leading to different location of the tensile fissure. In summary, the failure pattern of BPM-Crack is shear oblique and it is independent of model size. The localized failure and tensile fissure increase with model size, and they are affected by random seed.

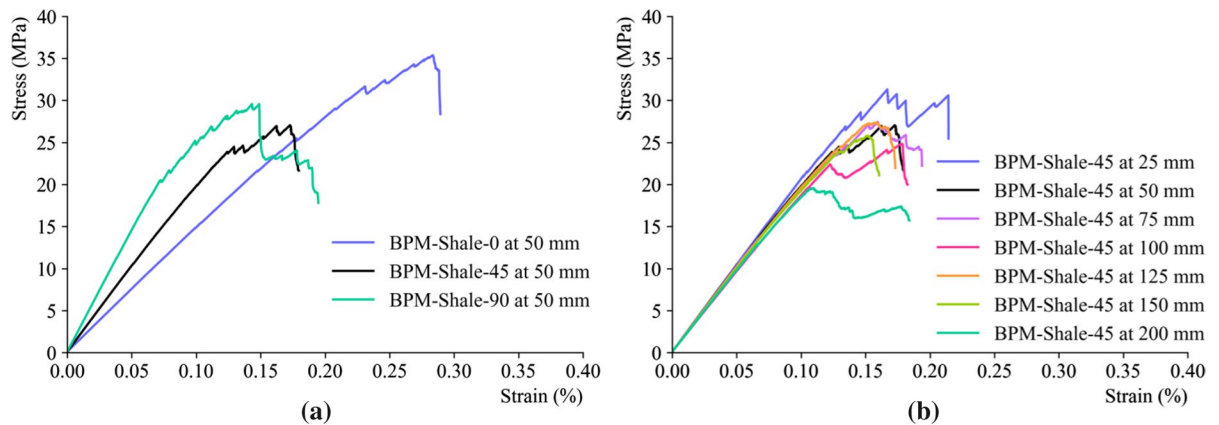
### 3.4 BPM-Shale

This study created the BPM-Shale using an assembly of bonded particles, smooth joints, and discrete fractures. There are three different orientations (0, 45, and 90°) and seven different sizes (25, 75, 100, 125, 150, and 200 mm) for the models of BPM-Shale. Each of the models has 10 realizations to eliminate the randomness of packing arrangement and crack distribution. Fig. 13 compares the stress-strain curves of BPM-Shale at some orientations and sizes as examples. From Fig. 13(a), the Young's modulus and UCS of 50 mm BPM-Shale is anisotropic. The Young's modulus increases with the increase of orientation angle. The UCS is maximum when the orientation angle is 0°, is medium when the orientation

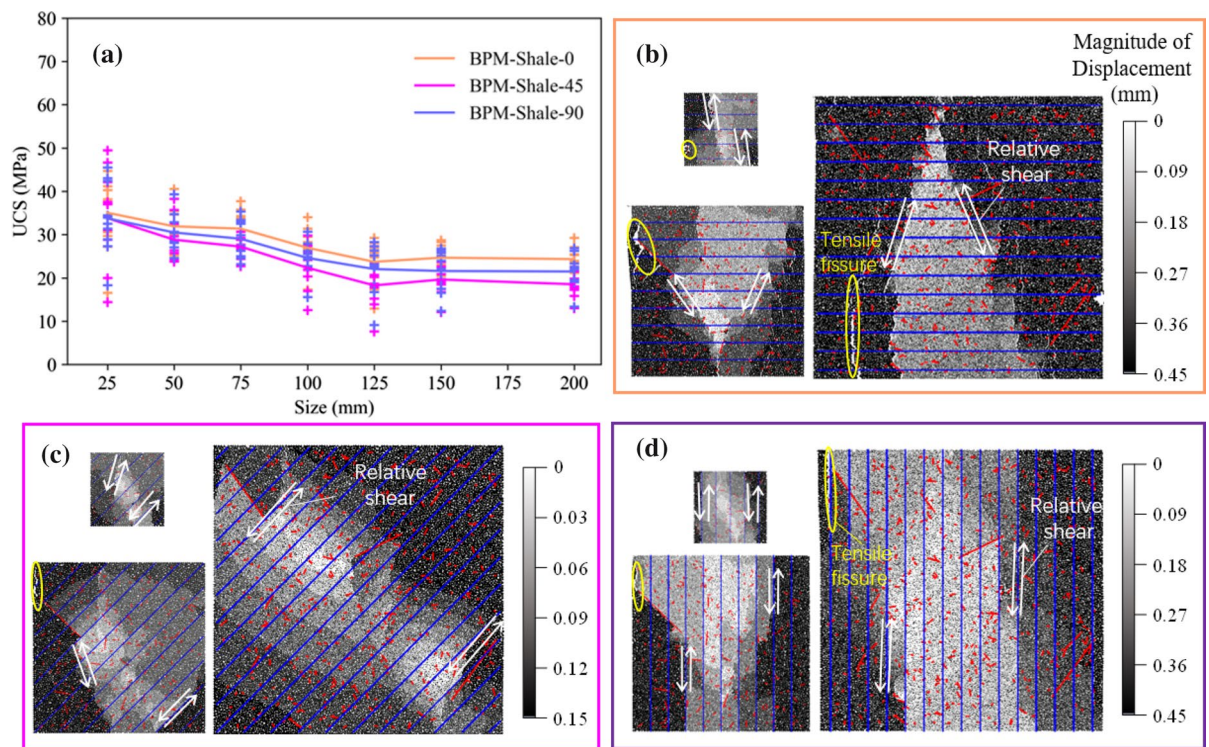
angle is 45°, and is minimum when the orientation angle is 90°. The anisotropic behavior is same to that of BPM-Bedding. From Fig. 13(b), the Young's modulus and UCS of BPM-Shale-45 decreases as the model size increases in the general case. The reduction of Young's modulus is small, but the decrease of UCS is significant. The decreasing trend is not strictly applied in all the model sizes due to the randomness of generating cracks. The decreasing size effect is same to that of BPM-Crack. Therefore, the BPM-Shale inherits anisotropy from BPM-Bedding and size effect from BPM-Crack.

Fig. 14 shows the uniaxial compression test results of the BPM-Shale: (a) variation of UCS with model sizes and orientations, (b) displacement magnitude of failed BPM-Shale-0 at random seed 1, (c) displacement magnitude of failed BPM-Shale-45 at random seed 1, and (d) displacement magnitude of failed BPM-Shale-90 at random seed 1. From Fig. 14(a), the dispersion of the UCS of BPM-Shale is very close to that of BPM-Crack. The dispersion is significantly more prominent than those of BPM-Matrix and BPM-Bedding. Moreover, the dispersion in BPM-Shale decreases with the increase of model size. The change of dispersion is like that of BPM-Crack but different than those of BPM-Matrix and BPM-Bedding. The significant dispersion of UCS and its change is caused by the randomness of crack distribution. It is evident that the average UCS is anisotropic and size dependent. The maximum, medium, and minimum UCS at each size occurs when the orientation is 0°, 90°, and 45°, respectively. The average UCS at the three orientations decreases when the model size increases from 25 to 200 mm and the rate of decrease diminishes.

As shown in Fig. 14(b) through (d), the displacement magnitude of failed BPM-Shale demonstrates that the failure pattern is dependent on the orientation and the model size. The general failure pattern



**Fig. 13** **a** stress–strain curves of 50 mm BPM-Shale at orientation angles of 0, 45, and 90° **b** stress strain curves of BPM-Shale-45 at different sizes



**Fig. 14** Uniaxial compression test results of the BPM-Shale: **a** variation of UCS with different model sizes and orientations, **b** displacement magnitude of failed BPM-Shale-0 at random

seed 1, **c** displacement magnitude of failed BPM-Shale-45 at random seed 1, **d** displacement magnitude of failed BPM-Shale-90 at random seed 1

of BPM-Shale is similar to that of BPM-Bedding. When the orientation is 0°, the oblique shear failure is across the bedding planes. When the orientation is 45°, the shear failure is along bedding planes. When

the orientation is 90°, the tensile failure occurs along the bedding planes. However, the existence of cracks causes the localized failure since the relative shear displacement tends to occur at the cracks. Moreover,

the localized failure leads to the development of the tensile failure. The influence of cracks is more significant in larger models as they might include larger cracks. Fig. 15 compares the failure mode for the 100 mm BPM-Shale-0, BPM-Shale-45, and BPM-Shale-90 at random seed from 1 to 5. It shows that the change of random seed affects the crack configuration, leading to different location of the tensile fissure. However, the general failure pattern is dependent on the orientation of bedding planes.

### 3.5 Combined Influence of Bedding Planes and Cracks

To further analyze the influence of bedding planes and cracks on the average UCS of BPM-Shale, Fig. 16 presents the results of BPM-Matrix, BPM-Crack, and BPM-Shale. The transformation assumes that the influences of bedding planes and cracks are additive. The influence of cracks (the deterioration rate  $D_{crack}$ ) is expressed as the relative decrease of UCS after the cracks are introduced,  $D_{crack} = (\text{UCS of BPM-Matrix} - \text{UCS of BPM-Crack}) / \text{UCS of}$

BPM-Matrix. Correspondingly, the influence of bedding planes (the deterioration rate of cracks  $D_{Bedding}$ ) is expressed as  $D_{bedding} = (\text{UCS of BPM-Crack} - \text{UCS of BPM-Shale}) / \text{UCS of BPM-Matrix}$ . As shown in Fig. 16, the deterioration rate  $D_{crack}$  is much higher than  $D_{Bedding}$ . Moreover,  $D_{crack}$  increases from 37 to 58% as the model size increase from 25 to 125 mm, and it maintains around 58% from 125 to 200 mm. Therefore, the influence of cracks increases with model size and the increase rate diminishes above 125 mm. However,  $D_{Bedding}$  is relatively stable as the increase of model size, except for at the size of 25 mm. This anomaly might be due to the large dispersion for small size models. When the orientation is  $0^\circ$ ,  $D_{Bedding}$  decreases from 9 to 5% as model size increases from 50 to 200 mm. When the orientation is  $45^\circ$ ,  $D_{Bedding}$  is around 14% for all sizes. When the orientation is  $90^\circ$ ,  $D_{Bedding}$  is around 11% as the model size increases from 50 to 200 mm. Therefore, bedding planes have a higher influence when the orientation is  $45^\circ$ . The influence is lesser when the orientation is  $90^\circ$  and least when the orientation is  $0^\circ$ .

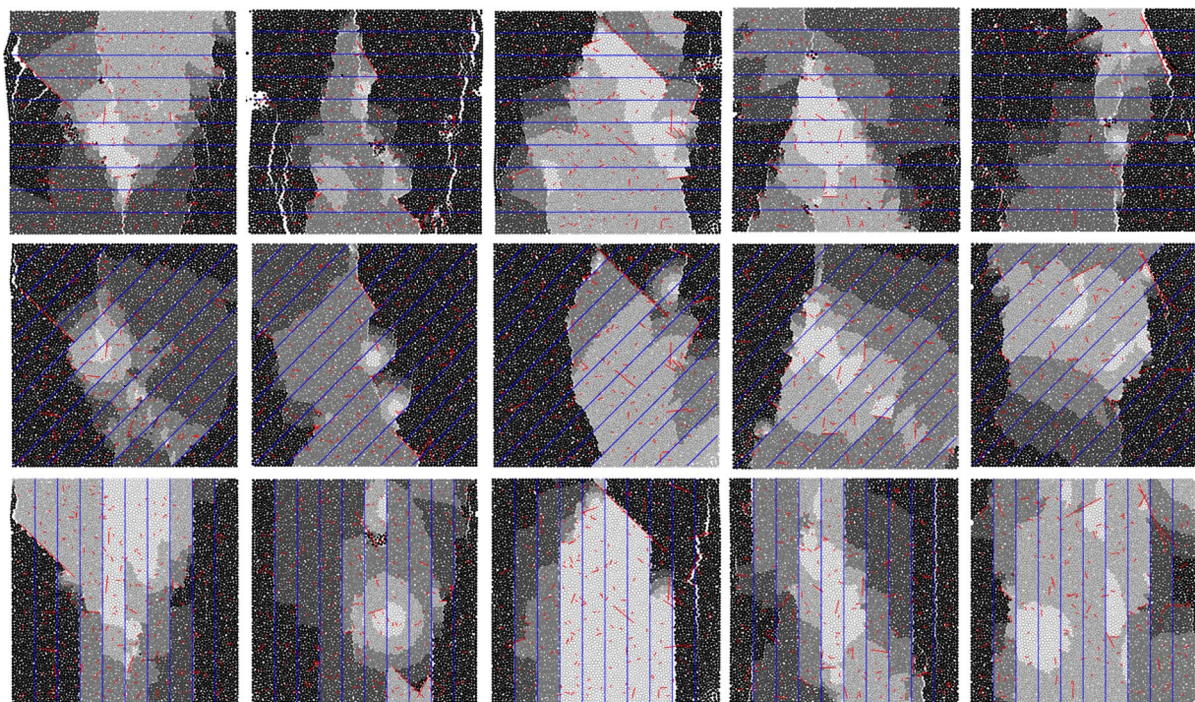


**Fig. 15** Failure mode comparison for the 100 mm BPM-Shale-0, BPM-Shale-45, and BPM-Shale-90 at random seed from 1 to 5 (from left to right)

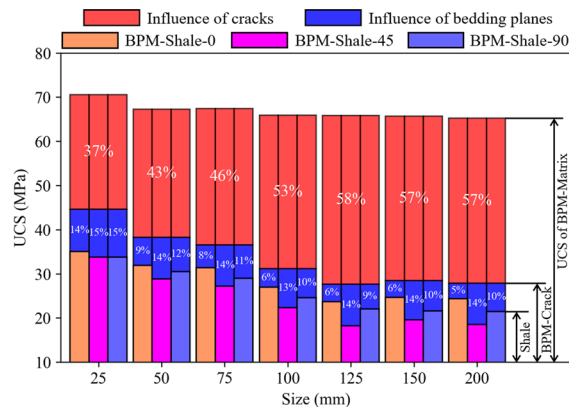


**Fig. 16** Influences of cracks and bedding planes on the UCS of the BPM models

Fig. 17 compares the influences of cracks and bedding planes on the displacement magnitude of the failed BPM models at the size of 100 mm. At the top left corner of BPM-Matrix, there was no fracture. At the same location of BPM-Crack and BPM-Bedding-0, a fracture occurred due to the cracks and bedding planes respectively. When the cracks and bedding planes coexist in BPM-Shale-0, the fracture is much larger in size. In addition, its shape is also related to the position of cracks and bedding planes. This result demonstrates that both the cracks and

bedding planes contribute to the development of fracture inside BPM-Shale-0. However, the amount of their contributions cannot be distinguished.

### 3.6 Extension of BPM-Shale to other Orientation Angles

Although the bedding plane were calibrated at three orientation angles ( $0^\circ$ ,  $45^\circ$ , and  $90^\circ$ ), we believe it had captured the anisotropy and it could be applied to other orientation angles. This study then created the BPM-Shale at  $15^\circ$ ,  $30^\circ$ ,  $60^\circ$ , and  $75^\circ$ . Each of the models has 10 realizations to eliminate the randomness of packing arrangement and crack distribution. Fig. 18 shows the average UCS of BPM-Shale at seven orientations (including  $0^\circ$ ,  $45^\circ$ , and  $90^\circ$ ). The UCS for each model size exhibits the “U-shaped” curve against the orientation angle. The BPM-Shale has the maximum UCS at  $\beta = 0^\circ$ , and the second largest at  $\beta = 90^\circ$ , and the minimum at  $\beta = 60^\circ$ . In addition, the UCS shows the decreasing size effect in all the orientation angles, and the decrease rate diminishes. It is concluded that the anisotropy and size effect coexist when the model size is small, the size effect disappears when the model size reaches to a certain size (125 mm here). The reason is that larger model contains more cracks, which making the model statistically homogeneous with respect to the influence of cracks. The

**Fig. 17** Influences of cracks and bedding planes on the displacement magnitude of the failed BPM models at the size of 100 mm and random seed 1

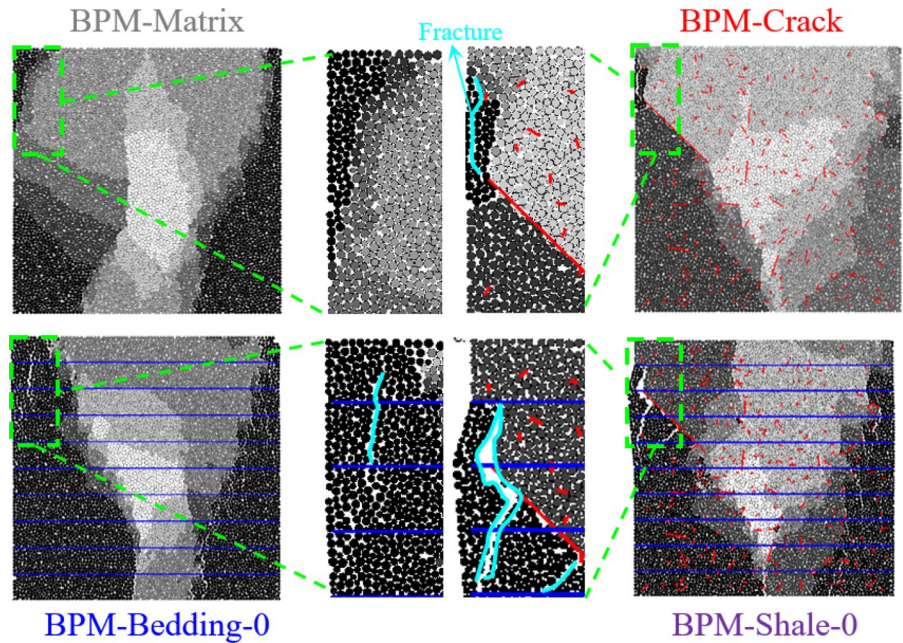
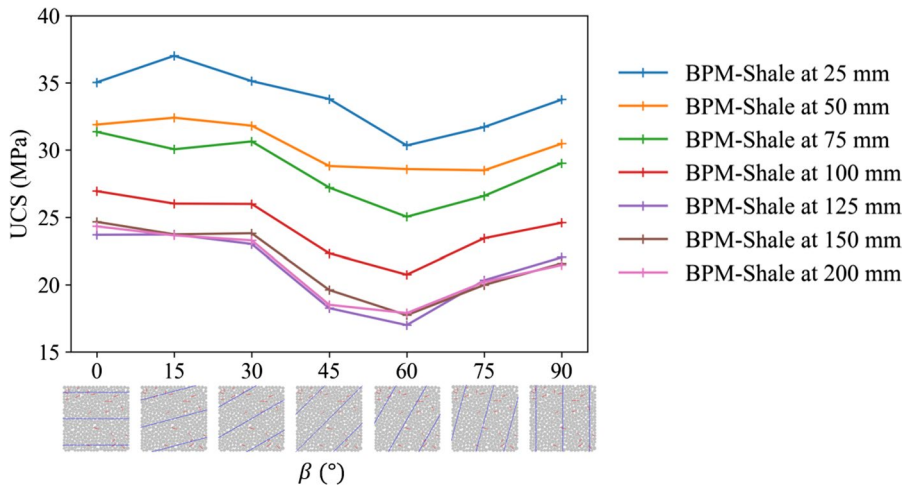


**Fig. 18** Anisotropy and size effect in the UCS of BPM-Shale



anisotropic and size dependent UCS of BPM-Shale follows the same trend in the experimental result of the transversely isotropic rock slate (Li et al. 2021).

#### 4 Conclusion

This research proposed a new BPM for transversely isotropic rock that integrates both anisotropy and size effect. Using shale as an example, the BPM-Shale contains shale matrix, bedding planes, and cracks that are modeled by bonded particles, smooth joints, and discrete fractures respectively. This study proposed a progressive part method to calibrate the bonded particles, smooth joints, and discrete fractures based on the mechanical properties of BPM-Matrix, BPM-Bedding, and BPM-Crack. This study used the calibrated BPM-Shale to investigate its size effect and anisotropy of UCS. A summary of the main conclusions is as follows:

- (1) The UCS of BPM-Matrix is isotropic and size independent. After the introduction of bedding planes, the UCS of BPM-Bedding is anisotropic. After the introduction of cracks, the UCS of BPM-Crack is size dependent. The combination of bedding planes and cracks make the UCS of BPM-Shale become anisotropic and size dependent. The UCS of BPM-Shale shows the “U-shaped” curve and the decreasing size effect.

- (2) The UCS variation is related to its failure pattern, which is affected by the bedding planes and cracks. The bedding planes influence the overall failure pattern, however the cracks cause the localized failure. The influence of bedding planes is consistent regardless of model size. Therefore, anisotropy exists at different model size. The influence of cracks increases with model size. Therefore, size effect exists at small-sized model, and it disappears when the model size reaches a certain size.
- (3) The numerical result of BPM-Shale corresponds well with the experimental result of slate (Li et al. 2021). The proposed model and its calibration procedure can be applied to model other transversely isotropic rocks for studying the size effect and anisotropy.

**Acknowledgements** This work was supported by the National Institute for Occupational Safety and Health (NIOSH) [grant number 200-2016-92214].

**Funding** The authors have not disclosed any funding.

**Data Availability** Enquiries about data availability should be directed to the authors.

#### Declarations

**Conflict of Interest** The authors declare that they have no known competing financial interests or personal relationships

that could have appeared to influence the work reported in this paper.

## References

- Alliot D, Boehler JP (1979) Evolution des propriétés mécaniques d'une roche stratifiée sous pression de confinement. In: Fourth International Congress on Rock Mechanics. pp 15–22
- Arora S, Mishra B (2015) Investigation of the failure mode of shale rocks in biaxial and triaxial compression tests. *Int J Rock Mech Min Sci* 79:109–123
- Attewell PB, Sandford MR (1974) Intrinsic shear strength of a brittle, anisotropic rock—I: experimental and mechanical interpretation. In: International journal of rock mechanics & mining sciences & geomechanics abstracts. pp 423–430
- Bajpayee TS, Pappas DM, Ellenberger JL (2014) Roof instability: what reportable Noninjury Roof Falls in underground coal mines can tell us. *Prof Saf* 59:57–62
- Bieniawski ZT (1968) The effect of specimen size on compressive strength of coal. *Int J Rock Mech Min Sci* 5:325–335
- Bonnet E, Bour O, Odling NE, Davy P, Main I, Cowie P, Berkowitz B (2001) Scaling of fracture systems in geological media. *Rev Geophys* 39:347–383
- Cundall P, Pierce M, Mas Ivars D (2008) Quantifying the size effect of rock mass strength. In: SHIRMS 2008: Proceedings of the first southern hemisphere international rock mechanics symposium. Australian Centre for Geomechanics. pp 1–15
- Donath F (1964) Strength variation and deformational behavior in anisotropic rock. *State Stress Earth's Crust* 281
- Duveau G, Shao JF, Henry JP (1998) Assessment of some failure criteria for strongly anisotropic geomaterials. *Mech. Cohesive-frictional mater. An Int. J Exp Model Comput Mater Struct* 3:1–26
- Goodman RE (1989) Introduction to rock mechanics. Wiley, New York
- Griffith A (1924) The theory of rupture. In: First international congress for applied mechanics. pp 55–63
- Hoek E, Brown ET (1980) Underground excavations in rock. CRC Press
- Hoskins JR, Horino FG (1969) Influence of spherical head size and specimen diameters on the uniaxial compressive strength of rocks. US Dept. of the Interior, Bureau of Mines
- Itasca Consulting Group (2019) PFC 6.0 Documentation
- Jaeger JC (1960) Shear failure of anisotropic rocks. *Geol Mag* 97:65–72
- Jin Z, Li W, Jin C, Hambleton J, Cusatis G (2018) Anisotropic elastic, strength, and fracture properties of Marcellus shale. *Int J Rock Mech Min Sci* 109:124–137. <https://doi.org/10.1016/j.ijrmms.2018.06.009>
- Kulatilake PHSW (1985) Estimating elastic constants and strength of discontinuous rock. *J Geotech Eng* 111:847–864. [https://doi.org/10.1061/\(ASCE\)0733-9410\(1985\)111:7\(847\)](https://doi.org/10.1061/(ASCE)0733-9410(1985)111:7(847))
- Kulatilake P (2017) Physical, empirical and numerical modeling of jointed rock mass strength. *Rock Mech Eng* 2:379–406
- Kulatilake PHSW, Ucpirti H, Wang S, Radberg G, Stephansson O (1992) Use of the distinct element method to perform stress analysis in rock with non-persistent joints and to study the effect of joint geometry parameters on the strength and deformability of rock masses. *Rock Mech Rock Eng* 25:253–274. <https://doi.org/10.1007/BF01041807>
- Kulatilake PHSW, Wang S, Stephansson O (1993) Effect of finite size joints on the deformability of jointed rock in three dimensions. *Int J Rock Mech Min Sci* 30:479–501. [https://doi.org/10.1016/0148-9062\(93\)92216-D](https://doi.org/10.1016/0148-9062(93)92216-D)
- Kulatilake PHSW, Malama B, Wang J (2001) Physical and particle flow modeling of jointed rock block behavior under uniaxial loading. *Int J Rock Mech Min Sci* 38:641–657. [https://doi.org/10.1016/S1365-1609\(01\)00025-9](https://doi.org/10.1016/S1365-1609(01)00025-9)
- Li K, Yin Z-Y, Han D, Fan X, Cao R, Lin H (2021) Size effect and anisotropy in a transversely isotropic rock under compressive conditions. *Rock Mech Rock Eng* 54:4639–4662
- McLamore R, Gray KE (1967) The mechanical behavior of anisotropic sedimentary rocks. *J Eng Ind* 89:62–73
- Mogi K (1962) The influence of the dimensions of specimens on the fracture strength of rocks: comparison between the strength of rock specimens and that of the earth's crust. *Bull Earthq Res Inst Univ Tokyo* 40:175–185
- Murphy MM (2016) Shale failure mechanics and intervention measures in underground coal mines: results from 50 years of ground control safety research. *Rock Mech Rock Eng* 49:661–671
- Niandou H, Shao JF, Henry JP, Fourmaintraux D (1997) Laboratory investigation of the mechanical behaviour of Tournemire shale. *Int J Rock Mech Min Sci* 34:3–16. [https://doi.org/10.1016/S1365-1609\(97\)80029-9](https://doi.org/10.1016/S1365-1609(97)80029-9)
- Park B, Min KB (2015) Bonded-particle discrete element modeling of mechanical behavior of transversely isotropic rock. *Int J Rock Mech Min Sci* 76:243–255
- Park B, Min KB, Thompson N, Horsrud P (2018) Three-dimensional bonded-particle discrete element modeling of mechanical behavior of transversely isotropic rock. *Int J Rock Mech Min Sci* 110:120–132. <https://doi.org/10.1016/j.ijrmms.2018.07.018>
- Pei J (2008) Strength of transversely isotropic rocks. Massachusetts Institute of Technology, Cambridge
- Potyondy DO (2012) A flat-jointed bonded-particle material for hard rock. In: 46th US rock mechanics/geomechanics symposium. 3: 1510–1519.
- Potyondy DO (2018) A flat-jointed bonded-particle model for rock. In: 52nd US Rock Mechanics/Geomechanics Symposium
- Potyondy DO (2019) Material-modeling support in PFC [fist-pkg6.6]. Itasca Consult. Group, Inc., Minneapolis, Minnesota, Tech. Memo. ICG7766-L (December 11, 2019)
- Poulsen BA, Adhikary DP (2013) A numerical study of the scale effect in coal strength. *Int J Rock Mech Min Sci* 63:62–71. <https://doi.org/10.1016/j.ijrmms.2013.06.006>
- Pratt HR, Black AD, Brown WS, Brace WF (1972) The effect of specimen size on the mechanical properties of unjointed diorite. *Int J Rock Mech Min Sci Geomech Abstr* 9:513–516

- Ramamurthy T (1993) Strength and modulus responses of anisotropic rocks. *Compr Rock Eng* 1:313–329
- Song H, Jiang Y, Elsworth D, Zhao Y, Wang J, Liu B (2018) Scale effects and strength anisotropy in coal. *Int J Coal Geol* 195:37–46
- Xue Y (2019) Time-dependent deformation and associated failure of roof in underground mines. West Virginia University, Morgantown. <https://doi.org/10.33915/etd.4077>
- Zhang Q, Zhu H, Zhang L, Ding X (2011) Study of scale effect on intact rock strength using particle flow modeling. *Int J Rock Mech Min Sci* 48:1320–1328

**Publisher's Note** Springer Nature remains neutral with regard to jurisdictional claims in published maps and institutional affiliations.

Springer Nature or its licensor holds exclusive rights to this article under a publishing agreement with the author(s) or other rightsholder(s); author self-archiving of the accepted manuscript version of this article is solely governed by the terms of such publishing agreement and applicable law.

## Terms and Conditions

Springer Nature journal content, brought to you courtesy of Springer Nature Customer Service Center GmbH (“Springer Nature”). Springer Nature supports a reasonable amount of sharing of research papers by authors, subscribers and authorised users (“Users”), for small-scale personal, non-commercial use provided that all copyright, trade and service marks and other proprietary notices are maintained. By accessing, sharing, receiving or otherwise using the Springer Nature journal content you agree to these terms of use (“Terms”). For these purposes, Springer Nature considers academic use (by researchers and students) to be non-commercial.

These Terms are supplementary and will apply in addition to any applicable website terms and conditions, a relevant site licence or a personal subscription. These Terms will prevail over any conflict or ambiguity with regards to the relevant terms, a site licence or a personal subscription (to the extent of the conflict or ambiguity only). For Creative Commons-licensed articles, the terms of the Creative Commons license used will apply.

We collect and use personal data to provide access to the Springer Nature journal content. We may also use these personal data internally within ResearchGate and Springer Nature and as agreed share it, in an anonymised way, for purposes of tracking, analysis and reporting. We will not otherwise disclose your personal data outside the ResearchGate or the Springer Nature group of companies unless we have your permission as detailed in the Privacy Policy.

While Users may use the Springer Nature journal content for small scale, personal non-commercial use, it is important to note that Users may not:

1. use such content for the purpose of providing other users with access on a regular or large scale basis or as a means to circumvent access control;
2. use such content where to do so would be considered a criminal or statutory offence in any jurisdiction, or gives rise to civil liability, or is otherwise unlawful;
3. falsely or misleadingly imply or suggest endorsement, approval , sponsorship, or association unless explicitly agreed to by Springer Nature in writing;
4. use bots or other automated methods to access the content or redirect messages
5. override any security feature or exclusionary protocol; or
6. share the content in order to create substitute for Springer Nature products or services or a systematic database of Springer Nature journal content.

In line with the restriction against commercial use, Springer Nature does not permit the creation of a product or service that creates revenue, royalties, rent or income from our content or its inclusion as part of a paid for service or for other commercial gain. Springer Nature journal content cannot be used for inter-library loans and librarians may not upload Springer Nature journal content on a large scale into their, or any other, institutional repository.

These terms of use are reviewed regularly and may be amended at any time. Springer Nature is not obligated to publish any information or content on this website and may remove it or features or functionality at our sole discretion, at any time with or without notice. Springer Nature may revoke this licence to you at any time and remove access to any copies of the Springer Nature journal content which have been saved.

To the fullest extent permitted by law, Springer Nature makes no warranties, representations or guarantees to Users, either express or implied with respect to the Springer nature journal content and all parties disclaim and waive any implied warranties or warranties imposed by law, including merchantability or fitness for any particular purpose.

Please note that these rights do not automatically extend to content, data or other material published by Springer Nature that may be licensed from third parties.

If you would like to use or distribute our Springer Nature journal content to a wider audience or on a regular basis or in any other manner not expressly permitted by these Terms, please contact Springer Nature at

[onlineservice@springernature.com](mailto:onlineservice@springernature.com)